Optics Letters

Higher-order cladding mode excitation of femtosecond-laser-inscribed tilted FBGs

Andreas Ioannou,[1,2] Antreas Theodosiou,[2] Kyriacos Kalli,[2,3] and Christophe Caucheteur[1,*]

[1]Electromagnetism and Telecommunication Department, Faculté Polytechnique, University of Mons, Boulevard Dolez 31, 7000 Mons, Belgium
[2]Photonics & Optical Sensors Research Laboratory (PhOSLab), Cyprus University of Technology, 31 Archbishop Kyprianos Street, 3036 Limassol, Cyprus
[3]e-mail: kyriacos.kalli@cut.ac.cy
*Corresponding author: christophe.caucheteur@umons.ac.be

Received 13 March 2018; revised 30 March 2018; accepted 30 March 2018; posted 5 April 2018 (Doc. ID 325968); published 27 April 2018

We study the modal behavior of plane-by-plane femtosecond laser fabricated tilted fiber Bragg gratings (FBGs). The focus is on the differential strain and temperature sensitivities between the cladding mode resonances of an nth grating order and those of the $(n-i)$th orders (with $i = 1-n$), which are collocated in the same wavelength range. Whereas the Bragg mode exhibits an axial strain sensitivity of 1.2 pm/με, we experimentally show that the strain sensitivity of ultrahigh-order cladding modes is negative and at −1.99 pm/με in the same spectral window. Using a finite element mode solver, the modal refractive index value is computed to be well below 1, thus confirming that these modes, in reality, are leaky modes.

OCIS codes: (060.3735) Fiber Bragg gratings; (060.2370) Fiber optics sensors.

https://doi.org/10.1364/OL.43.002169

Femtosecond laser fabrication of fiber Bragg gratings (FBGs) has received a great deal of attention over the past decade, with realizations that outperform what is conventionally feasible with the ultraviolet inscription processes [1,2]. Phase mask [3], point-by-point (PbP) [4], plane-by-plane (Pl-by-Pl) [5,6], and interferometric [7] inscription techniques have been used mainly for the photo-inscription of FBGs; all methods have their own benefits and shortcomings, therefore making them the choice for the fabrication process driven by issues related to the intended use (flexibility of design parameters, robustness in harsh environments, etc.) [8,9].

The focus of this Letter lies in the study of the higher-order cladding mode distribution and behavior in response to polarization, temperature, and axial strain changes. The presence of higher-order cladding mode resonances has been reported notably with extremely tilted fiber Bragg gratings (TFBGs) (>80°) [10]. TFBGs, similar to standard, uniform FBGs, are formed when a photo-inscription process takes place along the propagation axis of the optical fiber core, thus inducing a permanent and periodic modulation of its refractive index (RI). In addition to the core mode coupling at the Bragg wavelength, the angled RI modulation enables coupling from the core mode to hundreds (depending on the tilt angle value) of backward-propagating cladding modes [11]. We have recently reported that these TFBGs can be made using a direct write, Pl-by-Pl technique, which offers great flexibility in the periodicity and spatial extent of the RI modulation, allowing for highly controlled and selective coupling to cladding modes [12]. The excitation of high-order cladding mode resonances has also been achieved using long-period fiber gratings [13] with a periodicity in the range of 25 μm or using eccentric gratings usually made using the PbP technique [14,15].

In this Letter, we focus on even higher-order cladding modes, which we will call in the following ultrahigh-order cladding modes. They are generated with a higher-order TFBG ($n > 5$ where n is the grating order) produced in the C + L bands. Their location is ∼500 nm, blue-shifted from their corresponding Bragg peak and dependent on the particular TFBG order. We study the dependence of these modes on temperature and axial strain changes, and show that they are significantly different from those of lower-order modes located in the same wavelength range. A comparison between the experimental curves and numerical simulations obtained with a finite element mode solver allows us to confirm that these modes are leaky [16]. The unique feature of these modes lies is their strongly negative axial strain sensitivity, experimentally measured as −1.99 pm/με.

The investigated TFBGs were inscribed in FiberCore photosensitive single-mode optical fiber using the Pl-by-Pl method [5,6]. Fiber samples were mounted on two-axis air-bearing translation stages (Aerotech) allowing for controlled movement during the inscription process. The femtosecond laser system (HighQ laser femtoREGEN) generated 517 nm pulses of 220 fs duration, which were guided through a long working distance objective ×50 (Mitutoyo) and focused inside the fiber using a third translation stage. The inscribed planes had a width of ∼800 nm, while the other dimensions were adjusted by suitable translation stage motion, resulting in a three-dimensional refractive index change with a controlled plane length, depth,

and grating-plane angle. The pulse energy was set to 100 nJ, with a repetition rate of 50 kHz.

The TFBG transmitted amplitude spectra were recorded using a broadband light source (BBS) and an optical spectrum analyzer ([OSA] Yokogawa AQ6371C, 20 pm resolution). An in-line polarizer was placed in front of the TFBGs for measurement with polarized light. Schematic diagrams of the inscription and characterization setup are shown in Fig. 1.

Our choice of the TFBG parameters (periodicity and tilt angle) was driven by the wavelength range covered by the optical source and OSA and by our wish to see several grating orders in that range. For that reason, we inscribed an eighth-order TFBG located in the C + L bands. A tilt angle value of 7° was chosen, which is the value typically used for refractometric sensing in liquids with such gratings. The grating length was 5 mm. In Table 1, we present a calculation of the Bragg peak locations corresponding to the eighth TFBG in the C + L bands and their effective RIs, as calculated from the Sellmeier equation, with values corresponding to Ref. [17]. Considering the TFBG phase-matching condition,

$$\lambda^{j}_{\text{clad}} = \frac{[n_{\text{eff,co}} + n^{j}_{\text{eff, clad}}] * \Lambda_{\text{TFBG}}}{n_{\text{order}} * \cos(\theta)}, \quad (1)$$

where $\lambda^{j}_{\text{clad}}$ is the wavelength of the jth resonance, $n_{\text{eff,co}}$ and $n^{j}_{\text{eff, clad}}$, are the effective RI values for the core and the cladding mode, respectively, Λ_{TFBG} is the period of the grating, n_{order} is the order, and θ is the tilt angle.

From Eq. (1), we compute that the higher cladding mode resonances that overlap with the eighth-order spectrum belong to the fifth, sixth, and seventh orders. Orders above the fourth do not interfere because their last modes (corresponding to an effective RI of ~0.1) extend beyond 1700 nm and our ability to measure at that wavelength.

The transmitted amplitude spectrum measured for an eighth-order 7° TFBG is displayed in Fig. 2. The black curve mainly corresponds to the eighth grating order, while the red curve represents the spectrum relevant to the ninth-order grating. It can be seen that higher-order cladding modes are visible

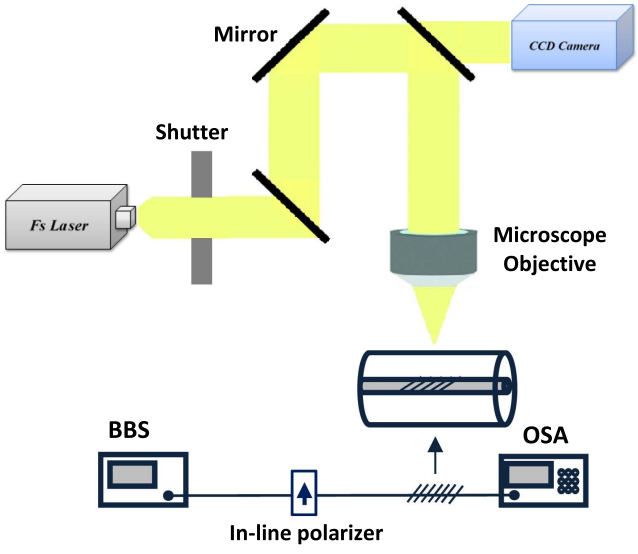

Fig. 1. Femtosecond laser inscription setup. Charge-coupled device (CCD), BBS, and OSA.

Table 1. Bragg Peak Position and Corresponding n_{eff} for Each Order

Order	Fifth	Sixth	Seventh	Eighth	Ninth
Bragg Peak (nm)	2509	2100	1806	1580	1410
RI	1.4344	1.4413	1.4455	1.4483	1.4512

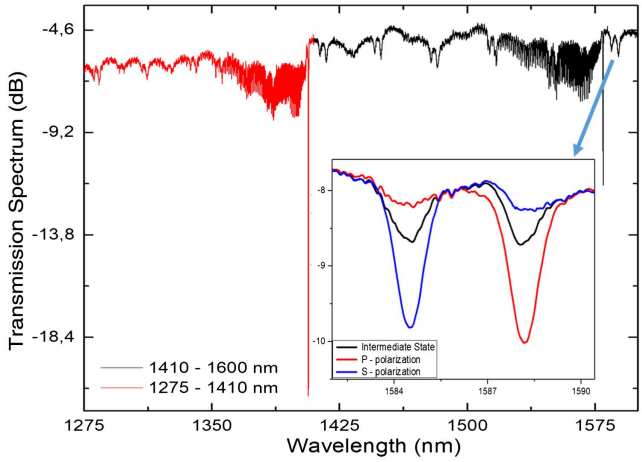

Fig. 2. Transmitted spectrum of an eighth-order 7° TFBG in the wavelength range 1410–1600 nm (black) and 1275–1410 nm (red). Inset: polarization dependence of an ultrahigh-order cladding mode.

in both parts of the spectrum. These higher-order cladding modes have strong polarization dependence, materialized by their double-peak shape, as shown in the inset of Fig. 2. The latter has been obtained for three different states of polarization, respectively, corresponding to the P- and S-polarized modes and the intermediate state with equal polarization contributions.

Taking into account that these modes are highly polarization dependent, a good read-out parameter is the polarization dependent loss (PDL) spectrum [18]. Figure 3 displays the transmitted amplitude spectrum and the corresponding PDL

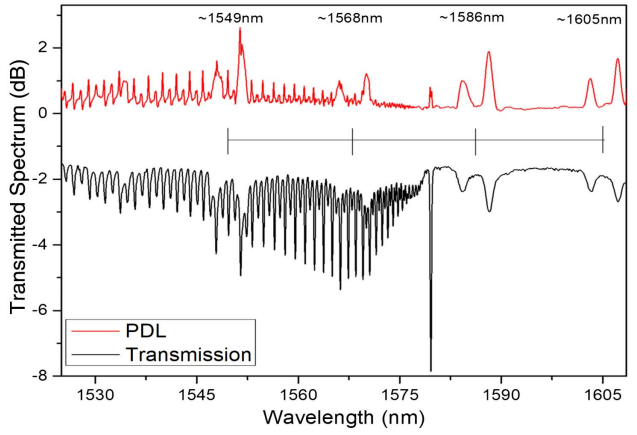

Fig. 3. Transmission spectra (black) and PDL (red) of the grating under study, where we visualize the higher-order cladding modes and, hence, determine the order of their origin.

acquired using a Luna optical vector analyzer (OVA CTe) in the C + L bands, yielding an alternative way to distinguish modes, even if they overlap with the modes of another order (here the eighth order) with greater resolution.

This will help to later identify the origin order of the higher-order cladding mode resonances. To help achieve this, we compare our experimental observations with numerical simulations conducted for the optical fiber geometry and laser modification used in this Letter.

The results of these simulations, focusing on the higher-order cladding mode resonances, are presented in Figs. 4 and 5. Figure 4 depicts the corresponding cladding mode positions computed from the real part of the effective RI given by the mode solver. Figure 5 presents the simulation results in a bar chart; the imaginary part of the complex RI (an image of the mode attenuation) is now computed as a function of its real part (converted to a wavelength based on the aforementioned phase-matching condition). These data are plotted on the same graph as the experimental spectrum so that a correlation can be made.

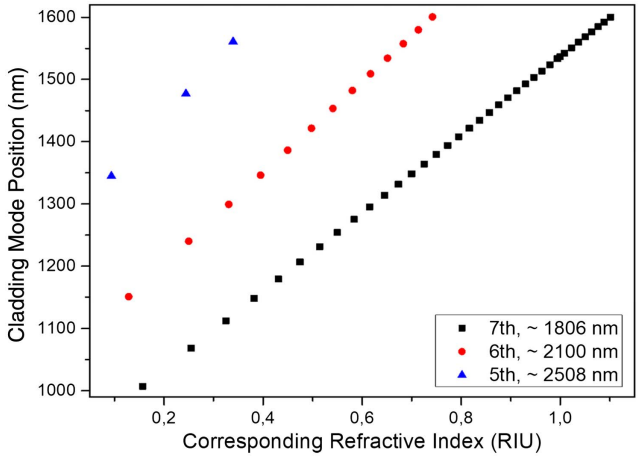

Fig. 4. Cladding mode positioning as a function of the effective RI (real part of the complex RI computed with FimmWave).

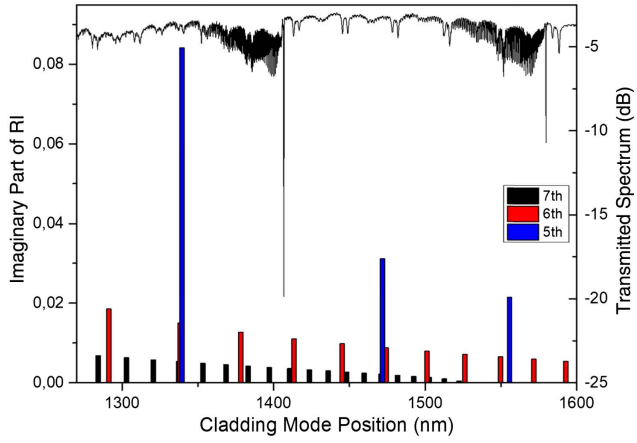

Fig. 5. Comparison between the experimentally acquired spectrum and the mode distribution computed by FimmWave displayed through the imaginary part of the complex RI.

Using this processed information, we can identify from which grating order the higher-order cladding modes originate. It is very important to note that for RIs close to 1, the corresponding cladding modes are irradiated. Indeed, they match the surrounding RI of air, resulting in their disappearance from the spectrum. The higher-order modes in the black part of Fig. 2 belong to the sixth-order mode (>1475 nm), since the seventh order is in the region of 0.9–1.0, and the fifth-order modes have RIs > 0.35. The modes of the red part (<1475 nm) belong mostly to the seventh order with a few sixth-order modes matching them.

Hence, given their effective RI values, the ultrahigh-order resonances that overlap in the spectrum correspond to leaky modes. This is also verified from their imaginary part, which increases greatly as the effective RI decreases and reaches 0.1 [18,19].

Now that the origin of the modes in the spectrum is well identified; we will present their sensitivity with respect to temperature and axial strain changes. For the temperature measurements, the gratings were placed in an oven accurate to 0.1°C. Figure 6 presents the obtained results for the Bragg resonance of the eighth, ninth, and tenth grating orders and the closest mode resonances belonging to higher grating orders. Using a linear regression on the measurement data, we recovered sensitivities of 9.56 pm/°C, 8.16 pm/°C, and 7.39 pm/°C for the eighth-, ninth-, and tenth-order Bragg peaks, respectively. Similarly, from each of their closest mode resonances, the sensitivities were 10.25 pm/°C, 9.01 pm/°C, and 8.23 pm/°C, respectively.

The strain responses of the eighth-, ninth-, and tenth-order Bragg gratings, as well with the closest mode resonances, are shown in Fig. 7. The TFBG fiber filter was fixed on a translation stage with 10 μm accuracy, while strain steps of 100 με were applied along the TFBG, up to 1000 με. The Bragg peaks exhibit sensitivities of 1.20 pm/με, 1.08 pm/με, and 0.97 pm/με for the eighth-, ninth-, and tenth-order gratings, respectively, whereas their closest higher-order cladding mode resonances show negative sensitivities of −1.99 pm/με, −1.76 pm/με, and −1.62 pm/με, respectively. The negative sensitivity of those particular modes is explained by considering that these modes have RIs below unity. Furthermore, we expect

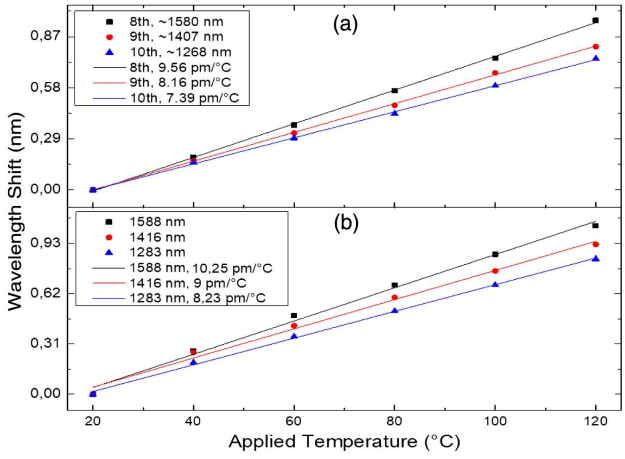

Fig. 6. (a) Temperature sensitivities of the Bragg modes and (b) their corresponding closest higher-order modes.

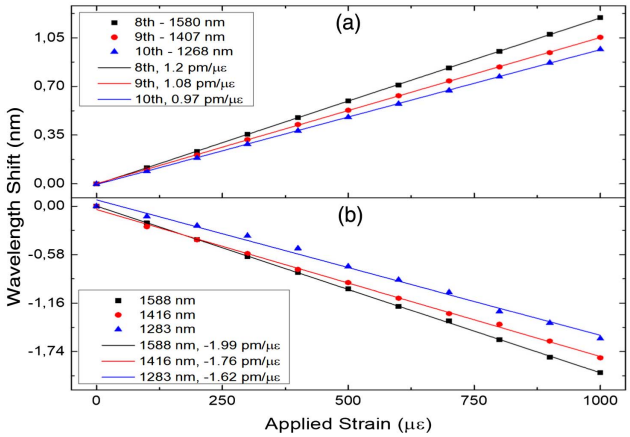

Fig. 7. (a) Strain sensitivities of the higher-order Bragg grating modes and (b) their corresponding closest higher-order cladding modes.

that at longer wavelengths the sensitivity will increase due to the differential nature of each order.

It is important to note, that the differential temperature sensitivity is below 1 pm/°C, whereas the differential strain sensitivity is up to 3 pm/με, almost three times larger than the Bragg peak sensitivity [20]. To the best of our knowledge, this is one of the best silica fiber cross-sensitivity performances to date.

We have shown the connection between higher-order cladding modes and leaky modes, along with their respective sensitivities to strain and temperature. We note that we can not only differentiate temperature and strain, but also use the cladding modes of the designed grating for refractometry (in for Ref. [12]), yielding a triple sensing device.

This Letter provides suitable information to reverse engineer the excitation of leaky modes and to control their presence in the wavelength spectrum. One may extract their corresponding RI and with the appropriately designed parameters to finally utilize them more efficiently.

Funding. H2020 European Research Council (ERC) (280161); Fonds De La Recherche Scientifique—FNRS (FNRS) (O001518F).

Acknowledgment. This Letter is funded by the Cyprus University of Technology for authors A. Theodosiou and K. Kalli, and by the Belgian F.R.S.-FNRS (associate research grant of C. Caucheteur and the EOS programme Charming).

REFERENCES

1. A. Martinez, M. Dubov, I. Khrushchev, and I. Bennion, Electron. Lett. **40**, 1170 (2004).
2. Y. Lai, A. Martinez, I. Khrushchev, and I. Bennion, Opt. Lett. **31**, 1672 (2006).
3. C. Hnatovsky, D. Grobnic, and S. J. Mihailov, Opt. Express **25**, 25435 (2017).
4. T. Geernaert, K. Kalli, C. Koutsides, M. Komodromos, T. Nasilowski, W. Urbanczyk, J. Wojcik, F. Berghmans, and H. Thienpont, Opt. Lett. **35**, 1647 (2010).
5. A. Theodosiou, A. Lacraz, M. Polis, K. Kalli, M. Tsangari, A. Stassis, and M. Komodromos, IEEE Photon. Technol. Lett. **28**, 1509 (2016).
6. A. Theodosiou, A. Lacraz, A. Stassis, C. Koutsides, M. Komodromos, and K. Kalli, J. Lightwave Technol. **35**, 5404 (2017).
7. B. E. A. Saleh and M. C. Teich, *Fundamentals of Photonics* (Wiley, 1991).
8. H. Chikh-Bled, K. Chah, Á. González-Vila, B. Lasri, and C. Caucheteur, Opt. Lett. **41**, 4048 (2016).
9. G. D. Marshall, R. J. Williams, N. Jovanovic, M. J. Steel, and M. J. Withford, Opt. Express **18**, 19844 (2010).
10. K. Zhou, L. Zhang, X. Chen, and I. Bennion, Opt. Lett. **31**, 1193 (2006).
11. J. Albert, L.-Y. Shao, and C. Caucheteur, Laser Photon. Rev. **7**, 83 (2013).
12. A. Ioannou, A. Theodosiou, C. Caucheteur, and K. Kalli, Opt. Lett. **42**, 5198 (2017).
13. F. Shen, C. Wang, Z. Sun, K. Zhou, L. Zhang, and X. Shu, Opt. Lett. **42**, 199 (2017).
14. K. Chah, D. Kinet, and C. Caucheteur, Sci. Rep. **6**, 38042 (2016).
15. J. Thomas, N. Jovanovic, R. Kramer, G. Marshall, M. Withford, A. Tünnermann, S. Nolte, and M. Steel, Opt. Express **20**, 21434 (2012).
16. A. W. Snyder and D. J. Mitchell, Opto-Electronics **6**, 287 (1974).
17. G. Wernicke, J. Appl. Math. Mech. **64**, 134 (1984).
18. C. Caucheteur, S. Bette, C. Chen, M. Wuilpart, P. Mégret, and J. Albert, IEEE Photon. Technol. Lett. **20**, 2153 (2008).
19. A. W. Snyder and J. D. Love, *Optical Waveguide Theory* (Snyder and Love, 1983), pp. 487–513.
20. G. P. Brady, K. Kalli, D. J. Webb, D. A. Jackson, L. Reekie, and J. L. Archambault, IEE Proc. Optoelectron. **144**, 156 (1997).